

# Design and Characterisation of Tissue-Mimicking Gel Phantoms for Diffusion Kurtosis Imaging

Ziyafer Gizem Portakal,<sup>1,2</sup> Sophie Shermer,<sup>3</sup> Emiliano Spezi,<sup>2,4</sup> Teresa Perrett,<sup>2</sup> Nina Tuncel,<sup>5</sup> and Jonathan Phillips<sup>6</sup>

<sup>1</sup>*Department of Physics, Science and Arts Faculty, Cukurova University, 01330, Adana, Turkey*

<sup>2</sup>*Department of Medical Physics, Velindre Cancer Centre, CF14 2TL, Cardiff, United Kingdom*

<sup>3</sup>*Department of Physics, College of Science, Swansea University, SA2 8PP, Swansea, United Kingdom*

<sup>4</sup>*School of Engineering, Cardiff University, CF24 3AA, Cardiff, United Kingdom*

<sup>5</sup>*Department of Physics, Science Faculty, Akdeniz University, 07058, Antalya, Turkey*

<sup>6</sup>*Institute of Life Science, College of Medicine, Swansea University, Swansea SA2 8PP, United Kingdom*

(Dated: September 2, 2016)

The purpose of the study was to create tissue-mimicking gel phantoms appropriate for diffusion kurtosis imaging (DKI). Diffusion coefficients, including the well-known apparent diffusion coefficient (ADC) and the diffusion coefficient based on the kurtosis model, as well as (excess) kurtosis values were experimentally determined for gels made of agar, agarose and polyvinyl alcohol (PVA). Although we observe an increase in kurtosis with the concentration of the gelling agents, the values obtained from diffusion-weighted magnetic resonance imaging (DW-MRI) were too low to mimic the range of values reported in the literature for various healthy and diseased tissues. To create tissue-mimicking gels phantoms with more realistic kurtosis values, different concentrations of glass microbeads were added. Experimental characterisation showed that realistic kurtosis values for a range of tissues may be obtained by varying the concentration of the gelling agents and glass microbeads appropriately. To assess the effect of adding glass microbeads on other key properties such as relaxation times, saturation recovery and multi spin-echo relaxometry experiments were performed on all gel phantoms. The gel phantoms were also examined using computed tomography (CT) to evaluate their homogeneity and observe the effect of glass microbeads on the CT numbers of the phantoms.

PACS numbers: 82.56.Lz, 82.56.Ub, 82.70.Dd  
Keywords: kurtosis, diffusion, MRI

## I. INTRODUCTION

Diffusion-weighted magnetic resonance imaging (DW-MRI) is an important non-invasive technique to obtain information about tissue microstructure by calculating quantities including the apparent diffusion coefficient (ADC), and in the more general case of diffusion tensor imaging (DTI), information on the diffusion anisotropy *e.g.* the fractional anisotropy (FA) [1]. By acquiring a series of images with varying the degrees of diffusion sensitisation, parametric maps can be computed allowing qualitative and quantitative assessment of the diffusion behaviour. The simplest model for water diffusion in tissue is a Gaussian random process [2, 3], leading to linear decay of the natural logarithm of the DW-MRI signal intensity with increasing degrees of diffusion sensitisation. However, due to the complex structure of most biological tissues, the diffusion displacement probability distribution can deviate substantially from a Gaussian form [4, 5]. Diffusion kurtosis imaging (DKI) aims to capture the degree to which such diffusion processes are non-Gaussian by replacing the mono-exponential model by quadratic exponential model with a (dimensionless) coefficient  $K$  quantifying the (excess) kurtosis, or simply the kurtosis.

As with all quantitative imaging modalities, the development and validation of imaging protocols and pulse sequences in the case of MRI are of utmost importance.

This necessitates the development of experimentally well-characterised tissue-mimicking phantoms that can be used repeatedly for calibration, development, testing, quality assurance and indeed understanding the physics governing the imaging observations [6, 7]. The main types of phantoms used in MRI studies are aqueous solutions and gels [8]. Although easy to prepare, aqueous solutions are not tissue-mimicking in many regards, having  $T_1$  (spin-lattice) and  $T_2$  (spin-spin) relaxation times that are approximately equal, unlike *e.g.* human tissue, for which the  $T_2$  values are typically much shorter than  $T_1$ . Additionally, having a container may be a disadvantage for multi-modal imaging studies such as advanced ultrasound techniques. Gel phantoms, on the other hand, can be prepared to mimic the  $T_1$  and  $T_2$  values of human tissues [7–14]. They are also relatively easy to make and use, cost-effective, reusable, leak-resistant and have a long lifetime when a preservative material is added to inhibit bacterial growth. For these reasons, water-based tissue-mimicking gels based on agar, agarose or polyvinyl alcohol cryogel (PVA-C) have been investigated extensively in the literature [7–14]. Seaweeds are the most common source of biological gelling agents, as agar and agarose. There are also synthetic gelling agents such as PVA, which require freeze-thaw cycles to be gelled into a cross-linked hydrogel. However, these gel phantoms have not been evaluated and optimised for DKI.

Phantoms may be tissue-mimicking in various aspects, and which properties are relevant depends on the appli-

cation. For example, in MRI, relaxation times similar to those of the tissues being modelled is often required. We may also wish to control the density and homogeneity or elastic properties of the phantom to match those of biological tissue. For DKI, gel phantoms must exhibit diffusion properties at room temperature comparable to those of healthy or diseased tissue at body temperature (as phantoms should be useful at room temperature) and have relaxation times similar to those of the tissues being modelled. The present study aims to address this to create tissue-mimicking gel phantoms appropriate for DKI by characterising the ADCs and kurtosis values and relaxation times of agar, agarose and PVA-C phantoms. We focus on creating isotropic kurtosis phantoms as a starting point for creating more complex phantoms that can model complex anisotropic diffusion in biological tissues such as brain [15–18] and prostate [19–22]. Both pure gels and gels with various concentrations of additives such as glass microbeads are characterised in terms of their diffusive properties (including kurtosis), relaxation times and CT numbers. The gels considered are liquids immersed in a macromolecular framework. As such the diffusion of the water molecules should be hindered by the presence of the macromolecular skeleton. The addition of glass microbeads further increases the barrier concentration and hence the non-Gaussianity of the diffusion process should increase with the addition of such glass microbeads.

## II. METHODS

### A. Phantom Preparation

Multiple gel phantoms were prepared using different gelling agents including agar (#A7002, Sigma-Aldrich, Dorset, UK), agarose (#A0169, Sigma-Aldrich, Dorset, UK) and PVA (99+% hydrolysis degree, #363146, Sigma-Aldrich, Dorset, UK) at the Cancer Research Wales Laboratories in Velindre Cancer Centre. Homogeneous gel phantoms were created at different concentrations using desired powders dissolved in 18.2 MΩ cm distilled water and heated up to 80 °C to 90 °C while mixing for 30-45 minutes. Diazolidinyl urea (DU) (#D5146, Sigma-Aldrich, Dorset, UK) was added into the mixtures at 6 mg per ml to prevent bacterial growth. Solidification and polymerisation of plain agar and agarose gels occurs overnight at room temperature. For PVA cryogels, gelation is induced by freeze-thaw (FT) cycles, which involve placing the PVA phantoms in a freezer at −20 °C for 10 hours and then leaving them at the room temperature (20 °C) for 14 hours. The effects of differences in preparation on imaging properties were discussed in the literature [14, 23, 24]. For this work four freeze-thaw cycles are used. For the gels with glass microbeads varying amounts of glass microbeads (#K20, 3M microspheres, Easy Composites Ltd., Staffordshire, UK) with diameters ranging from 30 μm to 90 μm were added. Fifteen plain gel phan-

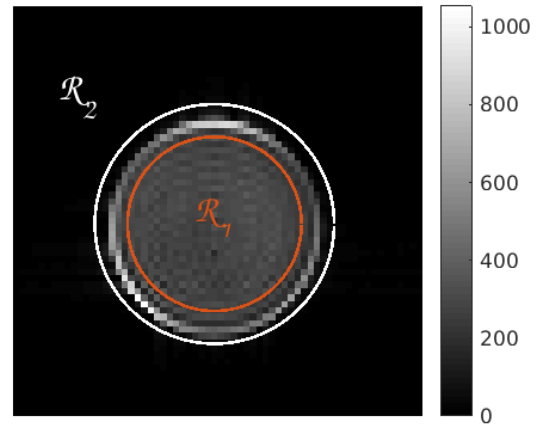


FIG. 1. Typical image with ROI selection  $\mathcal{R}_1$  (inner orange circle) and background selection  $\mathcal{R}_2$  (exterior of white circle) for background noise signal estimation.

toms (six agar, six agarose, three PVA-C) and twenty two gel phantoms containing glass microbeads in various degrees (fourteen agar, eight agarose) were created with a volume of 100 cm<sup>3</sup> each. Attempts to create PVA cryogels with the chosen microbead material were abandoned as the glass microbeads appeared to react with the PVA cryogels, resulting in a sticky gum-like material. For simplicity we shall refer to a gel with x g agar/agarose/PVA per 100 cm<sup>3</sup> as an x % agar/agarose/PVA gel.

### B. DW-MRI Measurements

DWI MRI data was acquired on a Siemens 3T Magnetom Skyra (Erlangen, Germany) MRI scanner using a combination of a 7 cm diameter loop and the four-channel spine coil to boost the diffusion-weighted signal for DW-MRI studies. The signal to noise ratio (SNR) of DW-MRI scans was tested using different single coils as well as dual coil combinations. In dual-coil imaging, two individual coils can be combined to function as a single coil with more elements allowing to increase volumetric coverage which improves signal acquisition efficiency and image quality. The loop and spine coil combination was chosen due to their best SNR results to calculate the diffusive properties [25].

Diffusion-weighted images were acquired using an in-house version of a spin-echo sequence with a pair of strong diffusion-weighting gradients straddling the 180° refocusing pulse known as Stejskal-Tanner sequence [26]. This sequence was developed because the SNR obtained with the standard vendor-provided diffusion sequence was determined to be too low for high (>2500 s mm<sup>-2</sup>)  $b$ -values. Images were acquired with  $b$ -values between 0 and 4000 s mm<sup>-2</sup> in steps of 500 s mm<sup>-2</sup> and the diffusion-encoding gradients applied in the slice-select direction.

The sequence was written in the Siemens **IDEA C++** programming environment. For the purposes of this investigation, which requires accurate phantom characterisation, the SNR and data quality were prioritised over rapid acquisition. Therefore, the scans were performed using normal  $k$ -space readout rather than single-shot echo planar imaging (SS-EPI) to avoid effects such as image blurring, localised signal loss and image distortions caused by eddy currents [28, 29], observed with the standard EPI diffusion sequence. The scan parameters were: field-of-view (FOV) = 100 mm  $\times$  100 mm, matrix size = 64 $\times$ 64,  $T_R$  = 3000 ms,  $T_E$  = 120 ms, readout bandwidth of 130 Hz/pixel, slice thickness 20 mm, single average.

In-house software written in **MATLAB** was used to analyse the images, including automatic region-of-interest (ROI) selection, background noise estimation and mean and pixel-by-pixel signal analysis. Thresholding was used to locate the sample and select a circular region of interest (ROI)  $\mathcal{R}_1$  about 80% of the diameter of the sample. For the purpose of estimating noise levels and SNR the background was defined as all voxels outside a circle approximately 1.2 times the diameter of the sample, as shown in Fig. 1. The ADC was calculated assuming linear decay of the natural logarithm of the DW-MRI signal intensity ( $I$ ) with increasing degrees of diffusion sensitisation

$$\log\left(\frac{I}{I_0}\right) = -bD, \quad (1)$$

where  $I_0$  is the signal intensity at  $b = 0$ ,  $D$  is the ADC, typically measured in  $\mu\text{m}^2/\text{s}$  and  $b$  is the degree of diffusion sensitisation given by

$$b = (\gamma g \delta)^2 (\Delta - \delta/3), \quad (2)$$

and typically measured in  $\text{s mm}^{-2}$ .  $\gamma$  is the gyromagnetic ratio,  $g$  is the amplitude of the diffusion-encoding gradient pulse,  $\delta$  is the duration of a single diffusion gradient and  $\Delta$  the delay between the gradients.

The kurtosis, a measure of the deviation of the diffusion propagator from a Gaussian form, was estimated using the quadratic exponential model

$$\log\left(\frac{I}{I_0}\right) = -bD + \frac{1}{6}b^2D^2K + \mathcal{O}(b^3), \quad (3)$$

where  $D$  is the diffusion coefficient and  $K$  the dimensionless (excess) kurtosis. To distinguish the diffusion coefficients for the linear and quadratic model we use  $D^{(1)}$  to denote the diffusion coefficient using the linear model (1) or ADC, and  $D^{(2)}$  to denote the diffusion coefficient using the quadratic model (3).

### C. MRI Relaxometry Measurements

Relaxometry measurements were performed on the same 3 T scanner using a four-channel spine coil. Spin-echo sequences with different echo and repetition times,

$T_E$  and  $T_R$ , respectively, were used to evaluate the relaxometric properties of the phantoms [27].  $T_1$  was determined using a saturation recovery protocol consisting of applying a custom spin echo sequence with a fixed  $T_E$  of 12 ms and  $T_R$  of 125, 250, 500, 1000, 2000, 3000, 4000, 6000, 7000 ms.  $T_2$  was determined using a vendor-supplied multi-spin echo sequence with  $T_E = n \cdot 15$  ms for  $n$  ranging from 1 to 32 and a long  $T_R$  of 6000 ms to ensure that the longitudinal magnetisation recovers sufficiently to avoid stimulated-echo effects. A 10 mm coronal slice through the phantom was selected with a FOV of 100 mm  $\times$  100 mm, a resolution of 128 pixels and readout bandwidth of 130 Hz/Px.

In-house software written in **MATLAB** was used to analyse the images. ROI selection was performed as described above. For the bulk analysis the mean and standard deviation of the signal over the ROI were determined for each image.  $T_1$  was determined by fitting the mean signal vs  $T_R$  according to

$$I(T_R) = I_0 \left[ 1 - \exp\left(-\frac{T_R}{T_1}\right) \right]. \quad (4)$$

$T_2$  was determined by fitting the mean signal vs  $T_E$  via

$$\log I(T_E) = -\frac{T_E}{T_2} + a_0. \quad (5)$$

$I_0$  and  $a_0$  are extra parameters necessary to fit the data related to the equilibrium magnetisation, which are not used. The number of echoes used for the linear fit was adjusted to avoid noise floor issues for long  $T_E$  for samples with short  $T_2$ . For most samples 16 echoes were fitted.

### D. CT Measurements

To systematically characterise the attenuation properties of gels made with different gelation materials and additives, and to assess the consistency and stability of the compounds over time, CT scans were performed and repeated four times over the period of the study. Two CT scanners (Siemens SOMATOM Sensation 64 and Siemens SOMATOM Definition AS) installed at the Velindre Cancer Centre and the Institute of Life Science, Swansea University, respectively, were used to measure the CT number of the phantoms in Hounsfield Units (HU) [30] for a peak voltage of 120 kV and tube current of 250 mA with 5 mm slice thickness in each scan. Mean HU were determined over an area of approximately 5  $\text{cm}^2$  using **ImageJ** software [45]. The CT scans are solely used to assess the consistency of the phantoms; the phantoms are not designed to be tissue-mimicking CT phantoms.

## III. RESULTS

A typical 100 ml phantom resulting from the preparation process described is shown in Fig. 2.

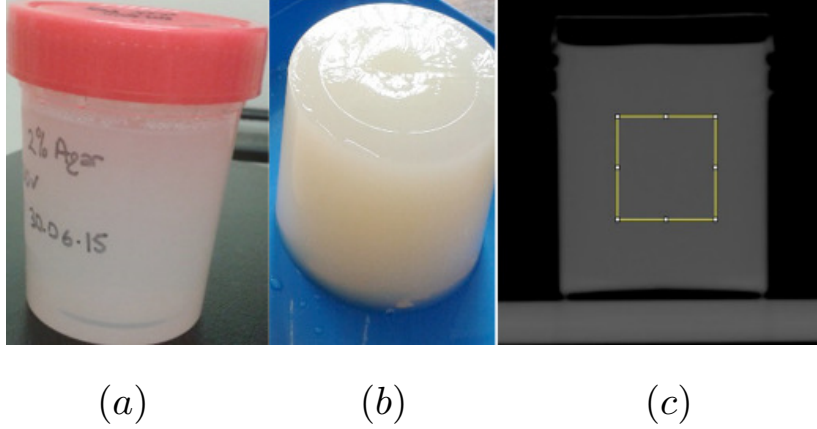


FIG. 2. Typical phantom (a) with and (b) without container and (c) CT image with ImageJ. The 100 ml cylindrical phantoms gels are approximately 5 cm in diameter and 5 cm in height.

### A. Diffusive Properties

The ADC ( $D^{(1)}$ ) obtained from linear fit of the signal intensity (Eq. (1)) in the diffusion-weighted image data as well as the diffusion coefficient  $D^{(2)}$  and kurtosis values obtained from the quadratic exponential fit (Eq. (3)) of the data are shown in Table I. For the linear exponential fit only the first four  $b$ -values ( $0 \text{ s mm}^{-2}$ ,  $500 \text{ s mm}^{-2}$ ,  $1000 \text{ s mm}^{-2}$  and  $1500 \text{ s mm}^{-2}$ ) were used, while all nine  $b$ -values ( $0 \text{ s mm}^{-2}$  to  $4000 \text{ s mm}^{-2}$ ) were used for the quadratic exponential fit.

Fig. 3 shows an example of the mean signal over the ROI  $\mathcal{R}_1$  as blue circles with error bars indicating the standard deviation of the signal, the linear fit of the logarithm of the signal (dashed blue line), the quadratic fit (solid red line) as well as the noise level, defined here as the mean signal over the exterior of the sample (dashed black line).

Fig. 4 shows that for all of the gels the ADC [ $D^{(1)}$  and  $D^{(2)}$ ] decrease slightly while the kurtosis increases with concentration of the gelling agent. However, even for high concentrations the kurtosis for pure gels is limited and does not cover the full range of values observed for biological tissue such as prostate [31–40]. The addition of glass microbeads increases the amount of kurtosis significantly, with the amount of kurtosis achieved for 2% agar gel with 2 g of glass microbeads (per 100 ml) exceeding 0.7. Furthermore, Fig. 5 shows that the kurtosis can be varied by adjusting the concentration of the glass microbeads. The amount of variation is particularly large for the 2% agar gels. Fig. 6 shows the concentration dependence of the ADC and kurtosis for PVA, showing that both  $D^{(1)}$  and  $D^{(2)}$  tend to decrease with the concentration of PVA while the kurtosis remains relatively constant around 0.42.

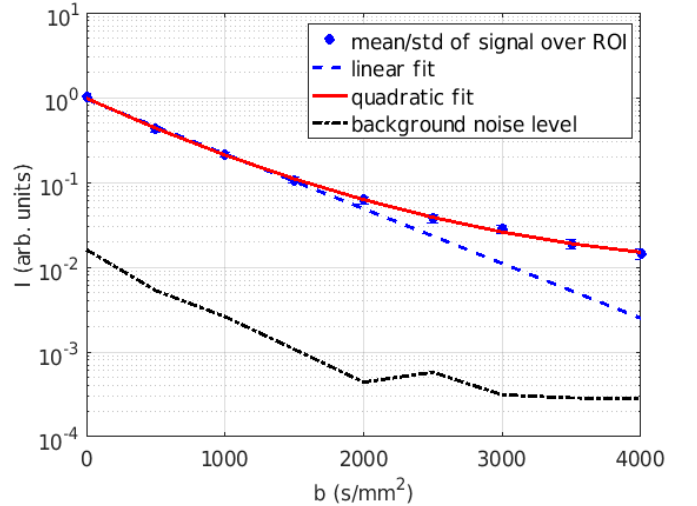


FIG. 3. Mean signal and standard deviation of the signal over the ROI  $\mathcal{R}_1$  (blue circles/error bars) as a function of the  $b$ -value as well as the linear fit (dashed blue line), the quadratic fit (solid red line) and the scaled background noise signal measured over  $\mathcal{R}_2$  (black dashed line) for a typical phantom (in this case the 2% agar sample with 0.1 g glass microbeads). The small error bars are consistent with the homogeneity of the samples observed in the CT scans.

### B. Relaxometric Properties

Figs 7 and 9 show that  $T_1$  decreases almost linearly with the concentration of the gelling agent for all gelling agents (agar, agarose, PVA) and  $R_2 = 1/T_2$  increases almost linearly, as expected. Furthermore, the addition of glass microbeads increases both  $T_1$  and  $R_2$ . Fig. 7

also shows that for agarose gel the addition of glass microbeads increases both  $T_1$  and  $T_2$  if the concentration of the gelling agent is kept fixed. For agar gels, on the other hand, we observe a decrease in  $T_1$  and an increase in  $R_2$  when beads are added but the concentration of agar is kept fixed. Fig. 8 shows that when the concentration of the gelling agent is fixed,  $T_1$  decreases with increasing microbead concentration while  $R_2$  tends to increase. The effect is less pronounced for agarose than for agar gels. Table II shows  $T_1$  and  $T_2$  relaxation times of all gel phantoms by comparing with the water.

#### IV. CT PROPERTIES

The CT properties of the gels are shown in Fig. 10. It is seen that HU slightly increases with the concentration of plain gels and it is almost stable for the ones with the same amount of glass beads. However, it is observed that HU decreases linearly when the concentration of beads are increased for agar gels but it is almost stable for the agarose ones. Table II shows detailed information on the effects of concentration, amount of glass beads, and gelling agent type for HU.

#### V. DISCUSSION

The results show that there is evidence of non-Gaussian diffusion in all of the gel phantoms, consistent with the idea that macromolecular structures formed by the gelling agents constitute barriers to the diffusive motion of the water molecules. The observed kurtosis values also increase with the concentration of gelling agent, at least for agar and agarose gels, but the kurtosis values for the pure gel phantoms are too low to mimic the values observed in the literature *in vivo* for a variety of human tissues.

The results further show that the addition of glass microbeads to the gels can significantly increase the observed kurtosis values, especially for agar gels, resulting in phantoms with kurtosis values matching those found *in vivo* more closely. This is consistent with the expectation that glass microbeads increase the barrier concentration and observations from other studies that increased barrier concentration increases kurtosis [6, 41].

The effect is more pronounced for agar gels. This may be due to the fact that agarose, one of the two principal components of agar, purified from agar by removing agar's other component, agaropectin, forms thermos reversible gels consisting of thick bundles of agarose chains linked by hydrogen bonds, with large pores holding water. Water in the large pores tends to relax more slowly than water in small pores because of the different relative

amounts surface and bulk water. It has also been noted that diffusion of particles in agarose gels is anomalous, with a diverging fractal dimension of diffusion when large particles become entrapped in the pores of the gel [42–44].

Characterisation of the gel phantoms using relaxometry to quantify the effect of the glass microbeads on the  $T_1$  and  $T_2$  times of the phantoms suggests that high bead concentrations tend to modify the  $T_1$  and  $T_2$  slightly, but the values remain suitable for tissue-mimicking phantoms and could easily be controlled by adjusting the concentration of the gelling agent or other additives such as  $T_1$  modifiers. CT results further suggest that it is possible to obtain stable and homogeneous phantoms with varying concentrations of glass microbeads.

#### VI. CONCLUSIONS

We investigated the diffusion properties of gel phantoms commonly used in MRI including agar, agarose and PVA gels with emphasis on the characterisation of non-Gaussian diffusion as quantified by the kurtosis. While pure gels were found to have low kurtosis values, we demonstrated that the kurtosis can be increased significantly by the addition of glass microbeads and controlled by varying the microbead concentration without significant changes to the consistency, homogeneity or relaxometry properties of the phantoms.

The work suggests that agar gel phantoms with glass microbeads in particular are promising materials for inexpensive but durable gel phantoms for DKI with tuneable diffusive and relaxometric properties. Future work includes the study of the effects of different types of glass microbeads and the design of more complex structured phantoms with non-isotropic, non-Gaussian diffusion for multi-modal imaging.

Tissue-mimicking DKI phantoms are an important tool to assess the diagnostic utility of DKI and its potential, e.g., for cancer patient screening, and to evaluate potential associations between DKI-derived parameters and clinical biomarkers.

#### ACKNOWLEDGMENTS

We gratefully acknowledge useful conversations with Geraint Lewis. ZGP acknowledges TUBITAK “The Scientific and Technological Research Council of Turkey” Project No. 1059B141400677 and Research Fund of Cukurova University, Project No. FDK-2014-2709 for financial support. SS acknowledges funding from a Royal Society Leverhulme Trust Senior Fellowship.

---

[1] Panagiotaki E, Chan RW, Dikaos N, Ahmed HU, O’Callaghan J, Freeman A, Atkinson D, Punwani

S, Hawkes DJ and Alexander DC 2015. Microstruc-

- tural characterisation of normal and malignant human prostate tissue with vascular, extracellular and restricted diffusion for cytometry in tumours magnetic resonance imaging *Invest. Radiol.* **50** 218-227.
- [2] Rosenkrantz AB, Padhani AR, Chenevert TL, Koh DM, De Keyser F, Taouli B and Le Bihan D 2015. Body diffusion kurtosis imaging: basic principles, applications, and considerations for clinical practice *J. Magn. Reson. Im.* **42** 1190-1202.
  - [3] Le Bihan D 2013. Apparent diffusion coefficient and beyond: what diffusion MR imaging can tell us about tissue structure *Radiology* **268** 318-22.
  - [4] Karger J 1985 NMR self-diffusion studies in heterogeneous systems *Adv. Colloid Interfac.* **23** 129-148.
  - [5] Jensen JH, Helpert JA, Ramani A, Lu H and Kaczynski K 2005 Diffusional kurtosis imaging: the quantification of non-Gaussian water diffusion by means of magnetic resonance imaging *Magnet. Reson. Med.* **53** 1432-1440.
  - [6] Phillips J and Charles-Edwards GD 2015 A simple and robust test object for the assessment of isotropic diffusion kurtosis *Magnet. Reson. Med.* **73** 1844-1851.
  - [7] Lavdas I, Behan KC, Papadaki A, McRobbie DW and Aboagye EO 2013 A Phantom for Diffusion-Weighted MRI? *J. Magn. Reson. Im.* **38** 173-179.
  - [8] Hattori K, Yusuke Ikemoto, Wataru Takao, Seiichiro Ohno, Takashi Harimoto, Susumu Kanazawa, Masataka Oita, Koichi Shibuya, Masahiro Kuroda and Hirokazu Kato 2013 Development of MRI phantom equivalent to human tissues for 3.0-T MRI *Med. Phys.* **40** 032303, 1711
  - [9] Laubach HJ, Jakob PM, Loevblad KO, Baird AE, Bovo MP, Edelman RR and Warach S 1998 A Phantom for Diffusion-Weighted Imaging of Acute Stroke *JMRI* **8** 1349-1354.
  - [10] Brewin MP, Birch MJ, Mehta DJ, Reeves JW, Shaw S, Kruse C, Whiteman JR, Hu S, Kenz ZR, Banks HT and Greenwald SE 2015 Characterisation of Elastic and Acoustic Properties of an Agar-Based Tissue Mimicking Material *Ann. Biomed. Eng.* **43** 2587-96
  - [11] Ogura A, Hayakawa K, Miyati T and Maeda F 2011 Imaging parameter effects in apparent diffusion coefficient determination of magnetic resonance imaging *Eur. J. Radiol.* **77** 185-188.
  - [12] Sack I, Gedat E, Bernarding J, Buntkowsky G and Braun J 2004 Magnetic resonance elastography and diffusion-weighted imaging of the sol/gel phase transition in agarose *J. Mag. Reson.* **166** 252-261.
  - [13] D'Souza WD, Madsen EL, Unal O, Vigen KK, Frank GR and Thomadsen BR 2001 Tissue Mimicking Materials for a multi-imaging modality prostate phantom *Med. Phys.* **28** 688-700.
  - [14] Dwihapsari Y, Sari DP and Darminto 2012 The assessment of consistency using penetrometer and apparent diffusion coefficient (ADC) value using diffusion weighted magnetic resonance imaging (DW-MRI) from polyvinyl alcohol (PVA) formed by freezing-thawing cycle *AIP Conf. Proc.* **1454** 53-56, 2012.
  - [15] Armitage PA, Bastin ME, Marshall I, Wardlaw JM and Cannon J 1998 Diffusion anisotropy measurements in ischaemic stroke of the human brain *Magn Reson Mater Phy* **6** 28-36.
  - [16] Oouchi H, Yamada K, Sakai K, Kizu O, Kubota T, Ito H and Nishimura T 2007 Diffusion Anisotropy Measurement of Brain White Matter Is Affected by Voxel Size: Underestimation Occurs in Areas with Crossing Fibers? *AJNR Am. J. Neuroradiol.* **28** 1102-1106.
  - [17] Shimony JS, McKinstry RC, Akbudak E, Aronovitz JA, Snyder AZ, Lori NF, Cull TS and Conturo TE 1999 Quantitative diffusion-tensor anisotropy brain MR imaging: normative human data and anatomic analysis *Radiology* **212** 770-784.
  - [18] Beaulieu C 2002 The basis of anisotropic water diffusion in the nervous system - a technical review *NMR Biomed.* **15** 435-455.
  - [19] Reinsberg SA, Brewster JM, Payne GS, Leach MO and deSouza NM 2005 Anisotropic Diffusion in Prostate Cancer: Fact or Artefact? *Proc. Intl. Soc. Mag. Reson. Med.* **13** 269.
  - [20] Xu J, Humphrey PA, Kibel AS, Snyder AZ, Narra VR, Ackerman JJ and Song SK 2009 Magnetic Resonance Diffusion Characteristics of Histologically Defined Prostate Cancer in Humans *Magnet. Reson. Med.* **61** 842-850.
  - [21] Bourne RM, Kurniawan N, Cowin G, Sved P and Watson G 2012 Microscopic Diffusion Anisotropy in Formalin Fixed Prostate Tissue: Preliminary Findings *Magnet. Reson. Med.* **68** 1943-8.
  - [22] Bourne R and Panagiotaki E 2016 Limitations and Prospects for Diffusion-Weighted MRI of the Prostate *Diagnostics(Basel)* **6** 21.
  - [23] Maksuti E, Widman E, Larsson D, Urban MW, Larsson M and Bjllmark A 2016 Arterial Stiffness Estimation by Shear Wave Elastography: Validation in Phantoms with Mechanical Testing *Ultrasound Med. Biol.* **42** 308-321.
  - [24] Surry KJM, Austin HJ, Fenster A and Peters TM 2004 Poly(vinyl alcohol) cryogel phantoms for use in ultrasound and MR imaging *Phys. Med. Biol.* **49** 5529-5546.
  - [25] Mitsouras D Hoge WS, Rybicki FJ, Kyriakos WE, Edelman A and Zientara GP 2004 Non-Fourier-Encoded Parallel MRI Using Multiple Receiver Coils *Magnet. Reson. Med.* **52** 321-328.
  - [26] Stejskal EO and Tanner JE 1965 Spin diffusion measurements: Spin-echoes in the presence of a time dependent field gradient *J. Chem. Phys.* **42** 288-292.
  - [27] Carneiro AAO, Vilela GR, de Araujo DB and Baffa O 2006 MRI relaxometry: methods and applications *Braz. J. Phys.* **36(1a)** 9-15.
  - [28] Farzaneh F, Riederer SJ and Pelc NJ 1990 Analysis of t2 limitations and off-resonance effects on spatial resolution and artefacts in echo-planar imaging *Magnet. Reson. Med.* **14** 123-139.
  - [29] Bammer R, Holdsworth SJ, Veldhuis WB and Skare ST 2009 New methods in Diffusion Weighted and Diffusion Tensor Imaging *Magn Reson Imaging Clin N Am.* **17(2)** 175-204.
  - [30] Thomas SJ 1999 Relative electron density calibration of CT scanners for radiotherapy treatment planning *Brit. J. Radiol.* **72** 781-786.
  - [31] Tamura C, Shinmoto H, Soga S, Okamura T, Sato H, Okuaki T, Pang Y, Kosuda S and Kaji T 2014 Diffusion Kurtosis Imaging Study of Prostate Cancer: Preliminary Findings *J. Mag. Reson. Im.* **40** 723-729.
  - [32] Mazzoni LN 2014 Diffusion-Weighted Signal Models in Healthy and Cancerous Peripheral Prostate Tissues: Comparison of Outcomes Obtained at Different b-values *J. Mag. Reson. Im.* **39** 512-518.
  - [33] Jambor I, Merisaari H, Taimen P, Bostrom P, Minn H, Pesola M and Aronen HJ 2015 Evaluation of Different Mathematical Models for Diffusion-Weighted Imaging of Normal Prostate and Prostate Cancer Using High b-

- Values: A Repeatability Study *Mag. Reson. Med.* **73** 1988-1998.
- [34] Roethke MC, Kuder TA, Kuru TH, Fenchel M, Hadaschik BA, Laun FB, Schlemmer HP and Stieltjes B 2015 Evaluation of Diffusion Kurtosis Imaging Versus Standard Diffusion Imaging for Detection and Grading of Peripheral Zone Prostate Cancer *Invest. Radiol.* **50** 483-489.
  - [35] Rosenkrantz AB, Sigmund EE, Johnson G, Babb JS, Mussi TC, Melamed J, Taneja SS, Lee VS and Jensen JH 2012 Feasibility and Preliminary Experience of a Diffusional Kurtosis Model for Detection and Assessment of Aggressiveness of Peripheral Zone Cancer *Radiology* **264** 126-135.
  - [36] Wang Q, Li H, Yan X, Wu CJ, Liu XS, Shi HB and Zhang YD 2015 Histogram analysis of diffusion kurtosis magnetic resonance imaging in differentiation of pathologic Gleason grade of prostate cancer *Urologic Oncol: Seminars and Original Investigations* **33(8)** 337.e15-24.
  - [37] Pang Y, Turkbey B, Bernardo M, Kruecker J, Kadoury S, Merino MJ, Wood BJ, Pinto PA and Choyke PL 2013 Intravoxel Incoherent Motion MR Imaging for Prostate Cancer: An Evaluation of Perfusion Fraction and Diffusion Coefficient Derived from Different b-Value Combinations *Magnet. Reson. Med.* **69** 553-562.
  - [38] Toivonen J, Merisaari H, Pesola M, Taimen P, Boström PJ, Pahikkala T, Aronen HJ and Jambor I 2015 Mathematical Models for Diffusion-Weighted Imaging of Prostate Cancer Using b Values up to 2000 s/mm<sup>2</sup>: Correlation with Gleason Score and Repeatability of Region of Interest Analysis *Magnet. Reson. Med.* **74** 1116-1124.
  - [39] Suo S, Chen X, Wu L, Zhang X, Yao Q, Fan Y, Wang H and Xu J 2014 Non-Gaussian water diffusion kurtosis imaging of prostate cancer *Magnet. Reson. Imaging.* **32** 421-427.
  - [40] Rosenkrantz AB, Prabhu V, Sigmund EE, Babb JS, Deng FM and Taneja SS 2013 Utility of Diffusional Kurtosis Imaging as a Marker of Adverse Pathologic Outcomes Among Prostate Cancer Active Surveillance Candidates Undergoing Radical Prostatectomy *AJR* **201(4)** 840-846.
  - [41] Chu-Lee L, Bennett KM and Debbins JP 2013 Sensitivities of statistical distribution model and diffusion kurtosis model in varying microstructural environments: a Monte Carlo study *J Magn Reson* **230** 19-26.
  - [42] Narayanan J, Xiong JY and Liu XY 2006 Determination of agarose gel pore size: Absorbance measurements vis a vis other techniques. *Journal of Physics:Conference Series* **28** 83-86.
  - [43] Fatin-Rouge N, Starchev K and Buffle J 2004 Size Effects on Diffusion Processes within Agarose Gels *Biophysical Journal* **86** 2710-2719.
  - [44] Ioannidis N 2009 Manufacturing of Agarose-Based Chromatographic Media with Controlled Pore and Particle Size *PhD Thesis, The University of Birmingham* 37.
  - [45] <http://www.imagej.net>

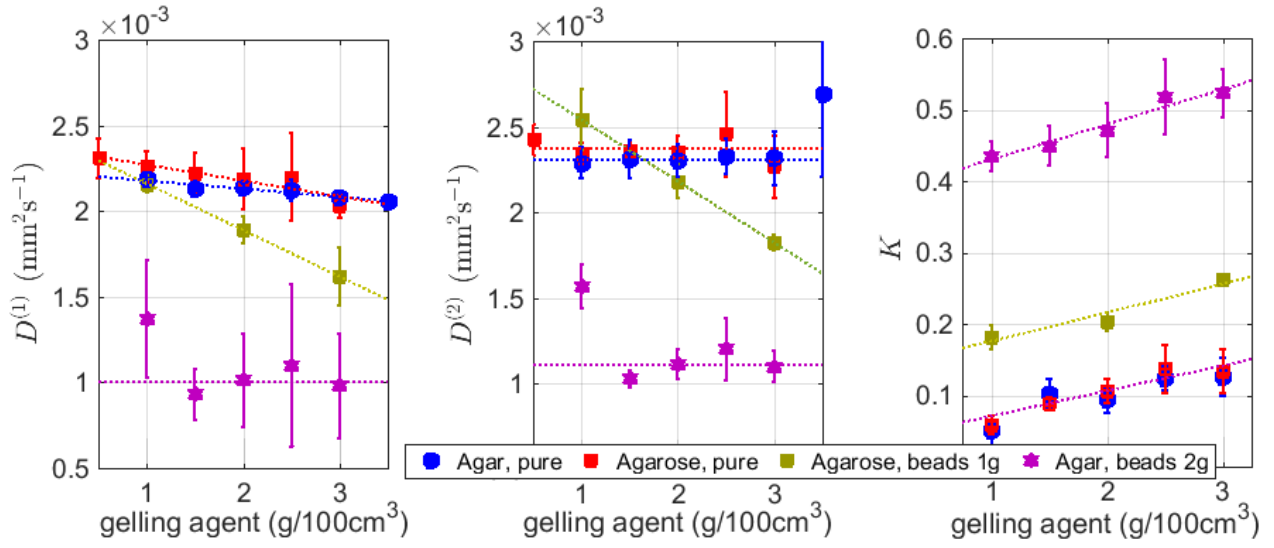


FIG. 4. The ADC,  $D^{(1)}$  and  $D^{(2)}$ , and  $K$  for gels with and without glass microbeads as a function of the gelling agent concentration.

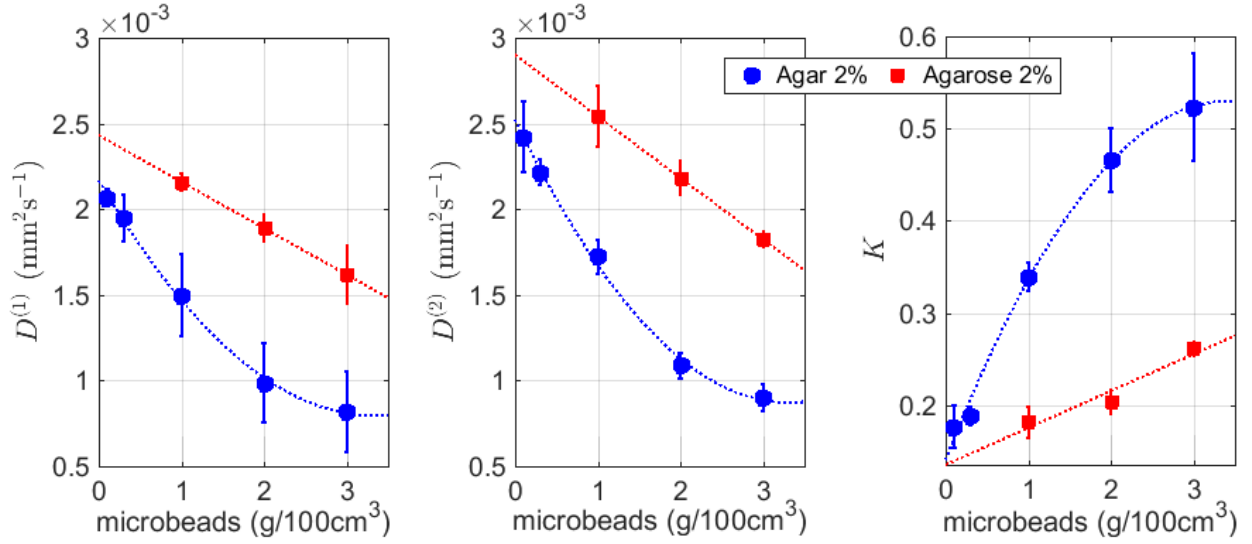


FIG. 5. The ADC,  $D^{(1)}$  and  $D^{(2)}$ , and  $K$  for 2% agar and 2% agarose gels as a function of the bead concentration.

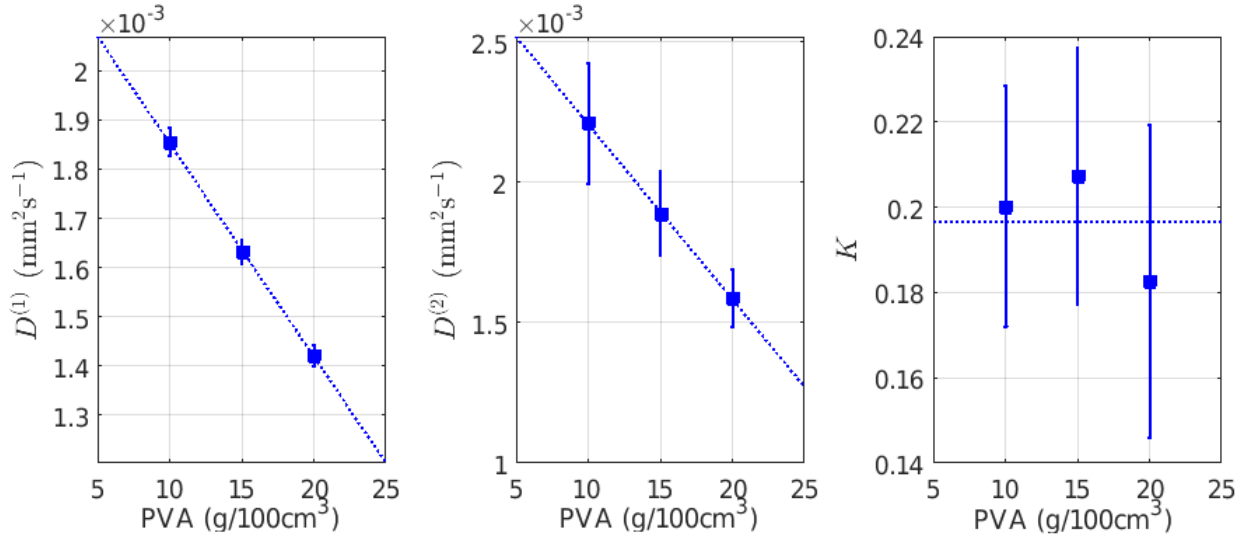


FIG. 6. The ADC,  $D^{(1)}$  and  $D^{(2)}$ , and  $K$  for pure PVA cryogels as a function of the concentration of PVA.



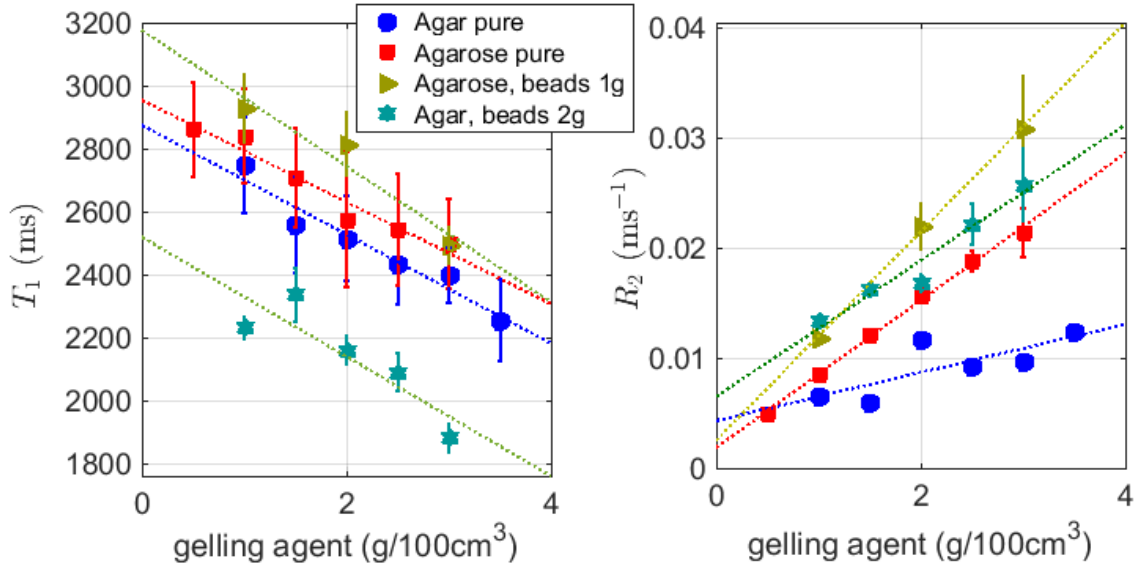


FIG. 7.  $T_1$  and  $R_2 = 1/T_2$  as a function of concentration of gelling agent.

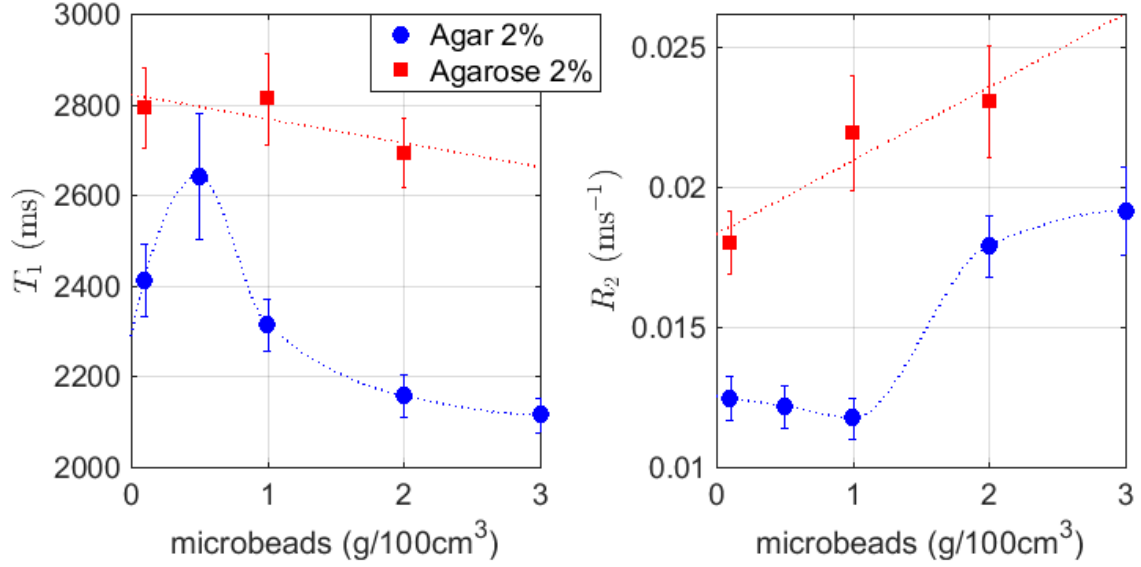


FIG. 8.  $T_1$  and  $R_2 = 1/T_2$  as a function of microbead concentration.

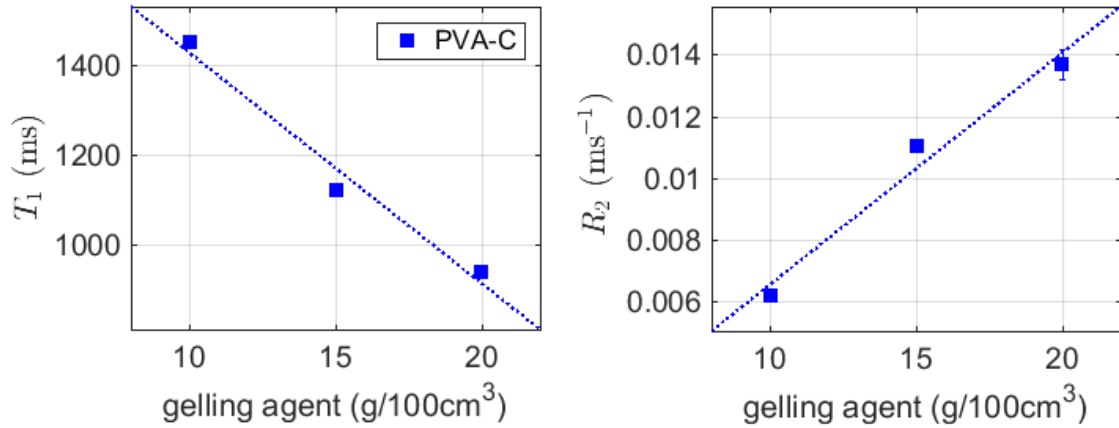


FIG. 9.  $T_1$  and  $R_2 = 1/T_2$  as a function of concentration of PVA.

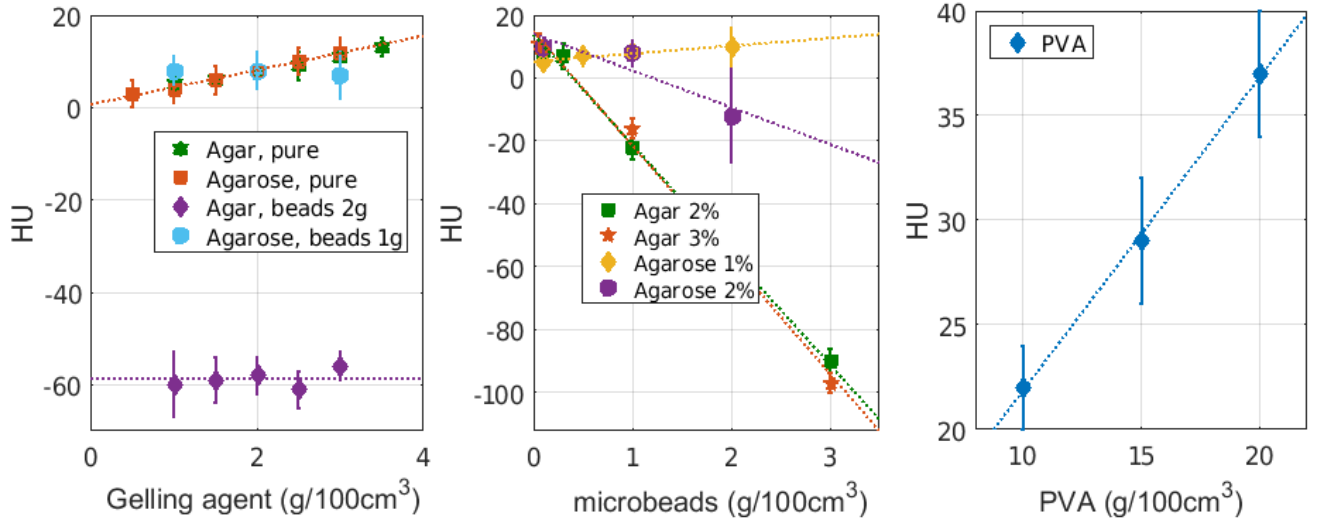


FIG. 10. HU as a function of concentration of concentration of gelling agents and beads.

	$D^{(1)}(\mu\text{m}^2/\text{s})$	$D^{(2)}(\mu\text{m}^2/\text{s})$	$K$
1.0% Agar	2184 (2140, 2227)	2288 (2198,2377)	0.050 (0.029, 0.710)
1.5% Agar	2133 (2090, 2177)	2308 (2196,2421)	0.102 (0.081,0.123)
2.0% Agar	2134 (2106, 2162)	2303 (2212,2394)	0.094 (0.076,0.111)
2.5% Agar	2121 (2060, 2183)	2329 (2223,2434)	0.124 (0.106,0.141)
3.0% Agar	2078 (2048, 2108)	2318 (2161,2474)	0.126 (0.100,0.152)
3.5% Agar	2055 (2016, 2095)	2694 (2210,3177)	0.216 (0.185,0.246)
0.5% Agarose	2308 (2191,2425)	2424 (2355,2513)	0.060 (0.043,0.078)
1.0% Agarose	2259 (2168,2350)	2344 (2283,2404)	0.059 (0.046,0.072)
1.5% Agarose	2222 (2102,2341)	2362 (2315,2409)	0.089 (0.080,0.098)
2.0% Agarose	2186 (2007,2364)	2355 (2261,2448)	0.106 (0.089,0.122)
2.5% Agarose	2198 (1944,2451)	2458 (2211,2706)	0.137 (0.103,0.170)
3.0% Agarose	2028 (1956,2100)	2267 (2088,2447)	0.133 (0.103,0.164)
10% PVA-C 4ft	1855 (1827,1883)	2210 (1995,2426)	0.200 (0.172,0.228)
15% PVA-C 4ft	1631 (1606,1656)	1890 (1740,2039)	0.207 (0.177,0.237)
20% PVA-C 4ft	1421 (1400,1443)	1586 (1484,1689)	0.183 (0.146,0.219)
1.0% Agar, 2.0g beads	1372 (1023,1720)	1573 (1443,1703)	0.435 (0.415,0.456)
1.5% Agar, 2.0g beads	923 (782, 1081)	1030 ( 983,1077)	0.449 (0.422,0.476)
2.0% Agar, 0.1g beads	2066 (2015,2117)	2421 (2217,2625)	0.177 (0.154,0.200)
2.0% Agar, 0.3g beads	1945 (1808,2081)	2215 (2142,2289)	0.189 (0.179,0.199)
2.0% Agar, 1.0g beads	1498 (1260,1737)	1723 (1622,1823)	0.330 (0.324,0.354)
2.0% Agar, 2.0g beads	986 (754,1218)	1115 (1026,1205)	0.466 (0.431,0.501)
2.0% Agar, 3.0g beads	818 (585,1053)	898 ( 819, 976)	0.523 (0.465,0.581)
2.5% Agar, 2.0g beads	1097 (621,1574)	1202 (1023,1381)	0.518 (0.466,0.570)
3.0% Agar, 0.05g beads	2012 (1941,2082)	2326 (2203,2449)	0.190 (0.175,0.204)
3.0% Agar, 0.1g beads	1913 (1812,2014)	2200 (2123,2278)	0.212 (0.203,0.222)
3.0% Agar, 1.0g beads	1227 (1011,1443)	1366 (1300,1431)	0.351 (0.331,0.371)
3.0% Agar, 2.0g beads	979 (676,1283)	1102 (1014,1190)	0.523 (0.490,0.556)
3.0% Agar, 3.0g beads	1124 (920,1328)	1231 (1069,1392)	0.449 (0.398,0.501)
3.5% Agar, 2.0g beads	1082 (836,1328)	1223 (1113,1332)	0.476 (0.443,0.509)
1.0% Agarose, 0.1g beads	2061 (1938,2184)	2340 (2252,2429)	0.168 (0.157,0.180)
1.0% Agarose, 0.5g beads	2252 (2218,2286)	2947 (2355,2739)	0.126 (0.101,0.151)
1.0% Agarose, 1.0g beads	1962 (1865,2060)	2227 (2125,2328)	0.196 (0.183,0.209)
1.0% Agarose, 2.0g beads	2257 (2118,2296)	2562 (2403,2721)	0.127 (0.118,0.156)
2.0% Agarose, 0.1g beads	2158 (2112,2205)	2542 (2365,2719)	0.182 (0.165,0.198)
2.0% Agarose, 1.0g beads	1890 (1811,1969)	2181 (2083,2278)	0.203 (0.190,0.216)
2.0% Agarose, 2.0g beads	1617 (1448,1785)	1824 (1780,1868)	0.262 (0.254,0.269)
3.0% Agarose, 1.0g beads	1355 (1196,1513)	1499 (1358,1640)	0.289 (0.248,0.330)

TABLE I. Diffusion and Kurtosis parameters (with 95% confidence intervals)

Gel Phantom Material	Density (kg/m <sup>3</sup> )	HU	$T_1$ (ms)	$T_2$ (ms)
1.0% Agar	1016	$5 \pm 3$	2748 (2595,2900)	153 (149,158)
1.5% Agar	1021	$6 \pm 3$	2557 (2403,2710)	169 (163,176)
2.0% Agar	1026	$8 \pm 3$	2514 (2379,2649)	86 (84,88)
2.5% Agar	1031	$9 \pm 3$	2430 (2302,2559)	109 (105,112)
3.0% Agar	1036	$11 \pm 3$	2396 (2306,2486)	103 (101,106)
3.5% Agar	1041	$13 \pm 2$	2253 (2125,2382)	80 (77,84)
0.5% Agarose	1011	$3 \pm 3$	2861 (2712,3011)	204 (197,212)
1.0% Agarose	1016	$4 \pm 3$	2839 (2688,2990)	117 (116,119)
1.5% Agarose	1021	$6 \pm 3$	2706 (2548,2864)	83 (81,85)
2.0% Agarose	1026	$8 \pm 3$	2574 (2360,2788)	64 (62,66)
2.5% Agarose	1031	$10 \pm 3$	2543 (2366,2720)	53 (51,56)
3.0% Agarose	1036	$12 \pm 3$	2498 (2355,2641)	47 (42,52)
10.0% PVA 4ft	1056	$22 \pm 2$	1453 (1441,1466)	162 (160,164)
15.0% PVA 4ft	1066	$29 \pm 3$	1122 (1110,1134)	91 (89,92)
20.0% PVA 4ft	1106	$37 \pm 3$	938 (925,951)	73 (71,76)
1.0% Agar, 2.0g beads	1036	$-60 \pm 7$	2230 (2196,2265)	75 (72,79)
1.5% Agar, 2.0g beads	1041	$-59 \pm 5$	2335 (2251,2419)	62 (60,64)
2.0% Agar, 0.1g beads	1027	$8 \pm 2$	2413 (2332,2494)	80 (76,86)
2.0% Agar, 0.3g beads	1029	$7 \pm 4$	2642 (2503,2781)	82 (77,88)
2.0% Agar, 1.0g beads	1036	$-22 \pm 4$	2314 (2257,2772)	85 (80,91)
2.0% Agar, 2.0g beads	1046	$-58 \pm 4$	2157 (2111,2203)	56 (53,59)
2.0% Agar, 3.0g beads	1056	$-90 \pm 4$	2116 (2078,2153)	52 (48,57)
2.5% Agar, 2.0g beads	1051	$-61 \pm 4$	2088 (2030,2147)	45 (42,49)
3.0% Agar, 0.05g beads	1036	$11 \pm 3$	2439 (2297,2582)	74 (69,79)
3.0% Agar, 0.1g beads	1037	$9 \pm 2$	2438 (2302,2573)	73 (68,78)
3.0% Agar, 1.0g beads	1046	$-16 \pm 3$	2179 (2099,2259)	47 (44,50)
3.0% Agar, 2.0g beads	1056	$-56 \pm 3$	1952 (1918,1986)	42 (39,46)
3.0% Agar, 3.0g beads	1066	$-97 \pm 3$	1879 (1834,1924)	39 (34,45)
3.5% Agar, 2.0g beads	1061	$-56 \pm 7$	2088 (2059,2117)	49 (40,58)
1.0% Agarose, 0.1g beads	1017	$5 \pm 3$	2756 (2656,2856)	105 (104,106)
1.0% Agarose, 0.5g beads	1021	$7 \pm 3$	2966 (2850,3081)	93 (88,100)
1.0% Agarose, 1.0g beads	1026	$8 \pm 3$	2926 (2818,3033)	85 (83,87)
1.0% Agarose, 2.0g beads	1036	$10 \pm 6$	2877 (2776,2978)	242 (238,246)
2.0% Agarose, 0.1g beads	1027	$10 \pm 3$	2793 (2703,2882)	56 (52,59)
2.0% Agarose, 1.0g beads	1036	$8 \pm 4$	2813 (2713,2912)	46 (42,50)
2.0% Agarose, 2.0g beads	1046	$-12 \pm 15$	2694 (2618,2769)	43 (40,48)
3.0% Agarose, 1.0g beads	1046	$7 \pm 5$	2493 (2435,2551)	33 (28,39)
Water	1000	$0 \pm 3$	$2825 \pm 365$	$2010 \pm 179$

TABLE II. Density, Hounsfield Units, and  $T_1$  and  $T_2$  relaxation times (with 95% confidence intervals)